A robust thermomechanical sintering simulation for 3D printed parts with internal lattices

Charles Manière, Joseph Sambasene Diatta, Thomas Grippi, Christelle Bilot, Guillaume Riquet, Sylvain Marinel

▶ **To cite this version:**

Charles Manière, Joseph Sambasene Diatta, Thomas Grippi, Christelle Bilot, Guillaume Riquet, et al.. A robust thermomechanical sintering simulation for 3D printed parts with internal lattices. Acta Materialia, 2024, pp.120024. ⟨10.1016/j.actamat.2024.120024⟩. ⟨hal-04586943⟩

HAL Id: hal-04586943

https://normandie-univ.hal.science/hal-04586943v1

Submitted on 24 May 2024

HAL is a multi-disciplinary open access archive for the deposit and dissemination of scientific research documents, whether they are published or not. The documents may come from teaching and research institutions in France or abroad, or from public or private research centers.

L'archive ouverte pluridisciplinaire **HAL**, est destinée au dépôt et à la diffusion de documents scientifiques de niveau recherche, publiés ou non, émanant des établissements d'enseignement et de recherche français ou étrangers, des laboratoires publics ou privés.

HAL Authorization

A robust thermomechanical sintering simulation for 3D printed parts with internal lattices

Charles Manière[1*], Joseph Sambasene Diatta[2], Thomas Grippi[1], Christelle Bilot[1], Guillaume Riquet[1], Sylvain Marinel[1]

1. Normandie Univ, ENSICAEN, UNICAEN, CNRS, CRISMAT, 14000, Caen, France
2. Assane Seck University, Ziguinchor, Sénégal

Keywords

Lattice ; Additive manufacturing ; Anisotropy ; Modeling ; Sintering

Abstract

Most parts printed with additive manufacturing used a bioinspired filling strategy with a dense shell and internal lattices. Such strategy helps optimizing the part strength/weight ratio through topology optimization and significantly improve the printing time and quality. However, simulate such complex porous inner structures would imply calculation instabilities and a colossal increase of the simulation time through the high number of degrees of liberty. Consequently, there is today no robust solution to simulate the sintering of printed parts with inner lattices, despite the fact that it represents the majority of the printed objects. This study circumvents this issue by a continuum approach that can simulate real parts and the complex lattice behavior with a computation time representing a small fraction of the sintering time. The lattice geometry is first simulated by a sub-model with identifies their effective moduli for different porosity. These effective moduli are then used to simulate the sintering in the lattices zones of the printed parts. The lattices also significantly decrease the inner part thermal conductivity. An additional sub-model is used to extract the effective lattice thermal conductivity by a simulation considering the thermal conduction in the lattice skeleton and the cavities thermal radiation and convection. A robust thermomechanical simulation is then possible to quickly and efficiently predict the parts firing with the developed thermal gradients and the distortions it results as well as the inherent anisotropy that greatly influence the final part dimensioning.

Graphical abstract

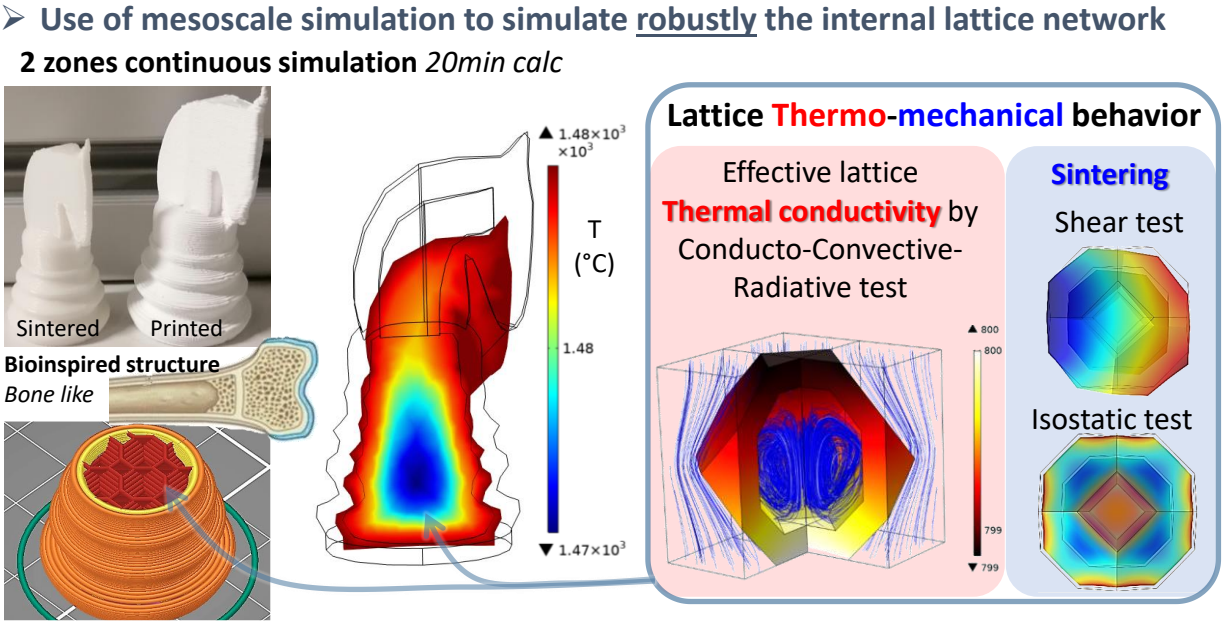

* Corresponding author: **CM**: Laboratoire de cristallographie et sciences des matériaux (CRISMAT), 6 Bvd du maréchal Juin 14050 CAEN CEDEX 4, France
Ph.: +33.2.31.45.13.69 ; *E-mail address*: charles.maniere@ensicaen.fr

Highlights

- Continuum approach for simulating the sintering of 3D printed shapes with lattices.
- Comprehensive experimental identification of anisotropic sintering behavior.
- Robust lattice scale simulations for accurate representation of lattice behavior.

Nomenclature

θ Porosity

$\dot{\theta}$ Porosity elimination rate (s^{-1})

ρ Relative density

$\underline{\sigma}$ Stress tensor ($N.m^{-2}$)

$\underline{s}$ Deviatoric stress tensor ($N.m^{-2}$)

$\underline{\dot{\varepsilon}}$ Strain rate tensor (s^{-1})

η Material viscosity (Pa.s)

η_0 Viscosity pre-exponential factor (Pa.s)

Q Deformability activation energy ($J.mol^{-1}$)

R Gas constant 8.314 ($J.mol^{-1}.K^{-1}$)

T Temperature (K)

$\dot{T}$ Heating rate (K/s)

φ Shear modulus

ψ Bulk modulus

φ_{eff} Effective lattice shear modulus

ψ_{eff} Effective lattice bulk modulus

θ_{ci} Initial critical porosity

θ_{cf} Final critical porosity

P_l Sintering stress ($N.m^{-2}$)

P_{lx}, P_{ly}, P_{lz} Anisotropic sintering stress terms ($N.m^{-2}$)

$\underline{\underline{\mathbb{1}}}$ Identity tensor

α Surface energy ($J.m^{-2}$)

r Particles radius (m)

$\dot{e}$ Trace of the strain rate tensor (s^{-1})

P Hydrostatic stress ($N.m^{-2}$)

I_1 Trace of the stress tensor ($N.m^{-2}$)

σ_r Hydrostatic applied stress ($N.m^{-2}$)

σ_{xz} Shear stress tensor component ($N.m^{-2}$)

$\dot{\varepsilon}_r$ Radial strain rate tensor component (s^{-1})

$\dot{\varepsilon}_z$ Axial strain rate tensor component (s^{-1})

$\dot{\varepsilon}_{xz}$ Shear strain rate tensor component (s^{-1})

V_g Shear velocity ($m.s^{-1}$)

G Grain size (m)

$\dot{G}$ grain growth rate ($m.s^{-1}$)

G_0 Initial grain size (m)

m Densification model grain size exponent

p Grain growth model grain size exponent

K Temperature dependent term of grain growth model ($m^{1+p}.s^{-1}$)

k_0 Pre-exponent term of grain growth model ($m^{1+p}.s^{-1}$)

Q_G Grain growth activation energy ($J.mol^{-1}$)

$a, \gamma, \zeta, c, c', c''$ Fitting constants

t Time (s)

q Imposed heat flux *($W.m^{-2}$)*

κ Thermal conductivity (W/(m.K))

κ_{eff} Effective lattice thermal conductivity (W/(m.K))

B Kinetic field model constant

Φ Master sintering curve integral parameter

MSC Master Sintering Curve

1. Introduction

In the realm of ceramic additive manufacturing, the integration of lattice structures represents a transformative advancement[1–6]. Lattices, intricate frameworks composed of interconnected struts, not only facilitate the creation of lightweight structures but also optimize structural integrity. This enables the production of complex geometries with improved strength-to-weight ratios and faster printing capabilities[7–10]. Exploring the vast potential of lattice designs in ceramic additive manufacturing opens new avenues for applications in fields ranging from aerospace to biomedical engineering, showcasing their versatility and impact across diverse industries[4,11–14].

In this context, understanding the sintering process of printed green specimens is paramount, given its critical impact on the final material dimensioning, deformations and properties. Experimental studies reveal distinctive features in the sintering of 3D-printed ceramic specimens, including interlayer porosity, anisotropy, and the presence of macro defects such as porosity and cracks[15–17]. Moreover, addressing the challenges posed by lattices, particularly in inner filling and support[10,18] structures, adds complexity to the sintering behavior.

The experimental specificity of sintering in 3D-printed ceramics necessitates advanced simulation tools mostly based on the finite element simulation[19]. The latter used the continuum theory of sintering[20,21] to model an effective compressive medium that reproduces the experimental sintering behavior. In general, sintering dilatometry is used to assess these models by methods like the “master sintering curve”[22,23], “kinetic field”[24,25], direct regression[26], or a combination of these approaches[27,28]. The sintering anisotropy is often reported in additive manufacturing and originates from interlayer porosity or particles alignment[29–36]. This should be incorporated through the moduli, viscosity and sintering stress[20,37,38]. However, a comprehensive formulation would require numerous specific sintering test to distinguish each individual parameter. Consequently, the anisotropy is

practically modeled by one of these parameters for instance through an anisotropic viscosity[29,32,36] or sintering stress[20,39].

One of the most challenging aspects, which constitutes the primary focus of this study, is the integration of porous lattice structures into the simulation. Several attempts have been made in the literature to simulate the heat transfer[40–42] and mechanics of lattices unit cells[36,43]. These simulations aid in comprehending the heat exchanges and mechanical behavior of different lattice structures. However, due to the considerable increase in the complexity of the real printed shape's geometry caused by lattices, direct simulation of their actual geometry becomes impractical in terms of computing time and stability. Consequently, an alternative approach needs to be explored.

In this work, lattice structures are simulated using an effective continuum approach. The real printed shapes can then be rapidly and robustly simulated by exhibiting different thermomechanical behavior in the lattice zones. Lattice-scale simulations are used to determine the effective sintering behavior and thermal conductivity of the lattices at varying porosities. The identification method is divided into three main stages. (i) The anisotropic sintering behavior, including the effect of macro porosity, is initially determined. These parameters can simulate the anisotropic sintering of printed shapes for 100% filling density printing[32,44]. (ii) The effective thermomechanical behavior of lattices is then determined through virtual tests on lattice unit cells. Shear and isostatic pressure tests are utilized to determine the sintering behavior, while conducto-convective-radiative tests are performed on lattice unit cells to determine the effective thermal conductivity. (iii) Finite element simulation of real shapes with a shell/lattice structure is used to test the feasibility and stability of such a comprehensive thermomechanical sintering simulation. In this study, 3D honeycomb lattices are investigated. This simulation is then utilized to anticipate the stability conditions of large-scale printed shapes and their deformation during heating and sintering.

2. Theory and calculations

In this section, the sintering model used in the finite element simulation tool and the corresponding analytical formulations are presented first. Then, the identification equations from dilatometry are depicted, encompassing the activation energy, viscosity, moduli parameters and sintering anisotropy introduced at the level of the sintering stress. The last part is dedicated to lattice scale simulation and the identification of the effective thermomechanical parameters for the lattices. These effective lattice parameters are used in the final sintering continuum simulation considering lattice/shell zones.

2.1. General finite element pressureless sintering model equations.

The continuum theory of sintering[20,21] defines the sintering behavior with the following equation:

$$\underline{\sigma} = 2\eta(T)\left(\varphi(\theta)\underline{\dot{\varepsilon}} + \left(\psi(\theta) - \frac{1}{3}\varphi(\theta)\right)\dot{e}\mathbb{1}\right) + P_l\mathbb{1} \quad (1)$$

with Skorohod's theoretical expression of the sintering stress;

$$P_l = \frac{3\alpha}{r}(1-\theta)^2 \quad (2)$$

and the strain rate invariant;

$$\dot{e} = \dot{\varepsilon}_x + \dot{\varepsilon}_y + \dot{\varepsilon}_z \quad (3).$$

The viscosity term and its inherent diffusional mechanisms grain growth sensitivity can be expressed by,

$$2\eta = \left(\frac{G}{G_0}\right)^m \eta_0 T \exp\left(\frac{Q}{RT}\right) \quad (4).$$

The shear and bulk moduli can be expressed by Skorohod's theoretical equations[20,21].

$$\varphi(\theta) = (1-\theta)^2 \quad (5)$$

$$\psi(\theta) = \frac{2}{3}\frac{(1-\theta)^3}{\theta} \quad (6)$$

The trace of strain rate tensor ($\dot{e}$) and the porosity elimination rate ($\dot{\theta}$) are related by the mass conservation equation.

$$\frac{\dot{\theta}}{1-\theta} = \dot{e} \quad (7).$$

Equations (1) to (7) can be implemented in a finite element code to simulate pressureless sintering. The strain rate formulation of equation (1) is particularly useful for simulation and analytical modeling. The latter is detailed in the following.

$$\underline{\dot{\varepsilon}} = \frac{1}{2\eta}\left(\frac{\underline{s}}{\varphi} + \frac{(P-P_l)}{3\psi}\underline{\underline{\mathbb{I}}}\right) \quad (8)$$

Ceramics are highly sensitive to grain growth, as it decreases the sintering stress (2) by increasing the curvature radii and through the creep grain growth sensitivity (4), where increased diffusion distances reduce the creep rates[27,45–47]. Consequently, the following grain growth model must be considered for polycrystalline ceramics.

$$\dot{G} = \frac{K(T)}{G^p} = \frac{k_0}{G^p} exp\left(\frac{-Q_G}{RT}\right) \quad (9)$$

One of the initial challenges in establishing a sintering model is to experimentally determine all input parameters for viscosity (η_0, Q), grain growth (k_0, p, Q_G). Skorohod's moduli can be used, but ideally, these moduli porosity functions $\varphi(\theta), \psi(\theta)$ may be determined experimentally through independent tests [48–50] or by corrective constant heating rate approaches using the master sintering curve [27,51–53].

2.2. Identification and simulation strategy

The sintering anisotropy and lattice porous structures are the two main challenges of the parameters identification and simulation. A specific strategy has been adopted to address this issue. Previous studies on anisotropic sintering of 3D printed materials [29,31,32,36] demonstrate that the activation energy and the porosity dependent moduli converge to same values regardless the printing direction. The identification process uses the porosity curves which is the volume of void on the total volume, this input parameter is the best to assess the sintering kinetic parameters in anisotropy case because it is independent on the porous morphology and only reflects the densification. In a new approach, inspired from Sarbandi *et*

al [39] and Olevsky [20] approaches, the viscosity and moduli are isotropic and the anisotropy is introduced from an anisotropic driving force. This greatly simplifies the identification where the viscosity and moduli are assessed from the porosity curves. The anisotropy is added in the end adjusting the sintering stress in the different directions. The other advantage is that the lattice structure simulation can be conducted using isotropic shear and bulk viscosities, which is much simpler than investigating the effect of anisotropy in these equations that would represent a high increase of the equation complexity.

2.3. Identification equation, case of pressureless sintering analytical formulation.

The finite element model uses tensors formulation, which is incompatible with the analytical model that requires ordinary differential equations for different specific cases like pressureless sintering. For pressureless isotropic sintering, the stress and strain rate tensors are simplified as,

$$\underline{\sigma} \equiv \begin{pmatrix} 0 & 0 & 0 \\ 0 & 0 & 0 \\ 0 & 0 & 0 \end{pmatrix} \quad ; \quad \underline{\dot{\varepsilon}} \equiv \begin{pmatrix} \dot{\varepsilon}_r & 0 & 0 \\ 0 & \dot{\varepsilon}_r & 0 \\ 0 & 0 & \dot{\varepsilon}_r \end{pmatrix} \text{ isotropic } \dot{e} = 3\dot{\varepsilon}_r \tag{10}.$$

Equation (1) becomes:

$$0 = 2\eta\left(\varphi\dot{\varepsilon}_r + \left(\psi - \frac{1}{3}\varphi\right)3\dot{\varepsilon}_r\right) + P_l \tag{11}.$$

We obtain the pressureless sintering analytic model [20];

$$\dot{\theta} = \frac{-P_l(1-\theta)}{2\eta\psi} \tag{12}$$

and by developing the equation (2) and (4) in (12), we obtain;

$$\dot{\theta} = \frac{-6\alpha(1-\theta)^3}{G^{m+1}\frac{\eta_0}{G_0^m}T\exp(\frac{Q}{RT})\psi} \tag{13}.$$

The latter sintering model with (9) can be used to conduct analytic modeling of the sintering curves. The first use here is to assess viscosity and moduli parameters from porosity curves. See the next identification sections.

2.4. *Identification of the powder sintering behavior by the constant heating rates calibration method.*

This method consists of conducting three dilatometry tests at different constant heating rates. Afterwards, the identification of the densification parameters is in two stages. The first stage consists of the independent identification of the sintering activation energy by the master sintering curves (MSC) and kinetic fields methods[22,24,25,54]. These methods are insensitive to the moduli porosity function.

The kinetic field method[24] consists of the linearization of equation (13) in the grain growth inactive zone and at fixed relative density. The slope of the following equation identifies the activation energy.

$$ln\left(T\dot{T}\frac{d\rho}{dT}\right) = B - \frac{Q}{RT} \tag{14}$$

Similarly, the MSC assumes a unique relative density function and the method consists of finding the activation energy at which, all heating rates relative density curves *vs* Φ term gathers in a unique curve.

$$\Phi = ln\left(\int_0^t \frac{exp\left(\frac{-Q}{RT}\right)}{T} dt\right) \tag{15}$$

The kinetic field and MSC methods have a similar principle and should converge to the same independent activation energy. It is advantageous to conduct both methods to detect eventual mechanism changes or grain growth nonlinearity in the MSC. These two methods can be done easily by using the SINTERLab home-made software.

The next step consists of the identification of the viscosity parameters and the correction of the bulk modulus by a direct regression method. The latter method is highly sensitive to the moduli function and is corrected to reproduce the MSC independent activation energy. The linear regression equation used for the direct method in intermediate stage sintering is the following.

$$Y = ln\left(\frac{-3(1-\theta)^3}{rT\dot{\theta}\psi}\right) = ln\left(\frac{\eta_0}{\alpha}\right) + \frac{Q}{RT} \tag{16}$$

The corrective methods uses the “modified Skorohod” moduli defined after.

2.5. Modified Skorohod moduli.

The theoretical moduli equation (5) and (6) corresponds to the dominant surface diffusion scenario with spherical porosity. In order to correct the initial stage high sintering reactivity with particle contact and sharp angles (low surface diffusion) an initial critical porosity (θ_{ci}) has been inserted in the moduli. Similarly, the intra-granular or macro-porosity that cannot be eliminated by sintering can be modeled in the bulk modulus through the final critical porosities (θ_{cf}) [27]. The modified Skorohod moduli are presented after.

$$\psi = a\frac{(\theta_{ci}-\theta)^{\gamma}}{(\theta-\theta_{cf})^{\zeta}} \tag{17}$$

$$\varphi = \left(1-\frac{\theta}{\theta_{ci}}\right)^{2} \tag{18}$$

These modified moduli have demonstrated their effectiveness in modeling real sintering behaviors. The final critical porosity (θ_{cf}) is particularly useful to predict the 3D printing defects involving macro-porosity. It is first introduced to predict the behavior of 3D printed silica[44], reused for the same material in ref[31], for alumina stereolithography[36], and it was presented in ref[27] as a corrective factor to predict final stage sintering microstructure development. The initial critical porosity (θ_{ci}) is one of the most useful parameter because it helps correcting the poor reactivity of theoretical moduli[55]. Most of the time, the latter involves an erroneously low sintering activation energy to compensate for their low reactivity. The initial critical porosity is then particularly effective at correcting the theoretical moduli to find the same activation energy as those obtained by independent moduli identification methods like the master sintering curve or kinetic field. The critical initial porosity was first formulated in ref[49] for the shear modulus, then the complete formulation was made for zirconia sintering behavior [27], it was then successfully used for spinel[53], flash SPS of zirconia [55], SPS [52] and pressureless sintering[36] of alumina, gas pressure sintering of silicon nitride[28]. For additive manufactured steel[56], tuning of θ_{ci} or the modulus exponent succeeds in reproducing

the sintering behavior. In some powders, both θ_{ci} and the moduli exponent should be tuned together to explain the experimental behavior[51].

For this article, θ_{ci} will be used to correct the moduli values with the MSC and θ_{cf} will be used to consider the 3D printing macro-porosity.

2.6. Final stage grain growth assessment.

Grain growth significantly decreases the sintering curve at final stage of sintering. Consequently, the grain growth behavior must be identified to reproduce the final stage sintering. Grain growth identification traditionally requires numerous interruption tests at different dwell times and for different temperatures [57]. In addition, the grain growth in high porosity regime may have a different sintering behavior than in fully dense regime[58–61]. To assess the grain growth in this particular regime and directly from the dilatometry data, we determine an inversion method based on equation (13) [27]. The following grain size estimative equation is used based on the dilatometry data and the already determined sintering parameters in intermediate sintering stage.

$$G = \left(\frac{-\frac{6\alpha G_0^m}{\eta_0}\exp(\frac{-Q}{RT})}{\dot{\theta}T} \frac{(1-\theta)^3}{\psi} \right)^{\frac{1}{m+1}} \quad (19).$$

As there are two main sintering mechanisms, two grain growth curves can be plotted, one for grain boundary diffusion (m=3) and one for lattice diffusion (m=2). The experimental final average grain growth is used to determine which mechanism is active.

2.7. Sintering anisotropy implementation.

The sintering anisotropy can be incorporated by different ways: the “viscosity” [29,32,36] and “sintering stress” [20,39] approaches as explained in the introduction. In this article, we choose to model the anisotropy through the sintering stress (P_{lx}, P_{ly}, P_{lz}). This approach enables to identify first the viscosity and moduli from shrinkage data and integrate the P_l anisotropy later

in the identification. In addition, P_l anisotropy will be a more stable solution for the final calculation that involves different moduli in the lattice and shell zones. Inspired by our previous work on sintering anisotropy of 3D printed green samples[29,32,36], the anisotropy will be assumed to be originated from the porosity architecture as no grains orientation is observed. Consequently, the anisotropy factor will be a function of the porosity that tends to 1 for full densification. The Pl expression is as follows.

$$\begin{cases} P_{lx} = Pl\,(1 + c\,\theta) \\ P_{ly} = Pl\,(1 + c'\theta) \\ P_{lz} = Pl\,(1 + c''\theta) \end{cases} \quad (20)$$

From equation (8), the anisotropic sintering curves can be plotted through the following analytic equations and with the expression (4) of the 2η term.

$$\dot{\varepsilon}_z = \frac{-P_{lz}}{(2\eta)3\psi} \quad (21)$$

$$\dot{\varepsilon}_y = \frac{-P_{ly}}{(2\eta)3\psi} \quad (22)$$

$$\dot{\varepsilon}_x = \frac{-P_{lx}}{(2\eta)3\psi} \quad (23)$$

With (2η), the viscosity expression described in equation (4).

2.8. Lattices effective modeling strategy.

Based on sintering dilatometry, all the modeling parameters will be identified for the simulation of 3D printed samples with fully dense filling strategy. To take into account the inner lattice filling of the shapes, the elemental lattice geometry will be simulated mechanically in deformation by shear tests to identify the effective shear modulus and by hydrostatic tests for the bulk modulus. Finally, a thermal model will be used to determine the lattice effective thermal conductivity.

The main study procedure is summarized in figure 1. The 3D printed shape used to illustrate this kind of lattice/shell simulation is reported in figure 1a. This geometry mimics the bone structure with a porous/shell architecture. The filling strategy uses 3D honeycomb lattices with

a filling density of 15%. This kind of lattice can be easily printed by FDM and is made of a truncated octahedron structure. The latter elemental lattice geometry is used for the lattice scale simulations that are reported in figure 1b.

For the sintering behavior, the shear and bulk moduli are determined by shear and hydrostatic tests on the truncated octahedron structure. The mechanical lattice sub-models are aimed at reproducing the fragile structure of the lattices. The simulation tests are made for different structure porosity and the moduli are determined by the measurement of the shear/hydrostatic strain rate. Because the lattice effective moduli represent the behavior of an equivalent compressible continuum, the applied stress has been calculated based on the force on the elemental cube face area.

Concerning the thermal model, a heat flux is imposed to record the developed temperature difference by the simulation. The details on the calculation of the moduli and conductivity is depicted below.

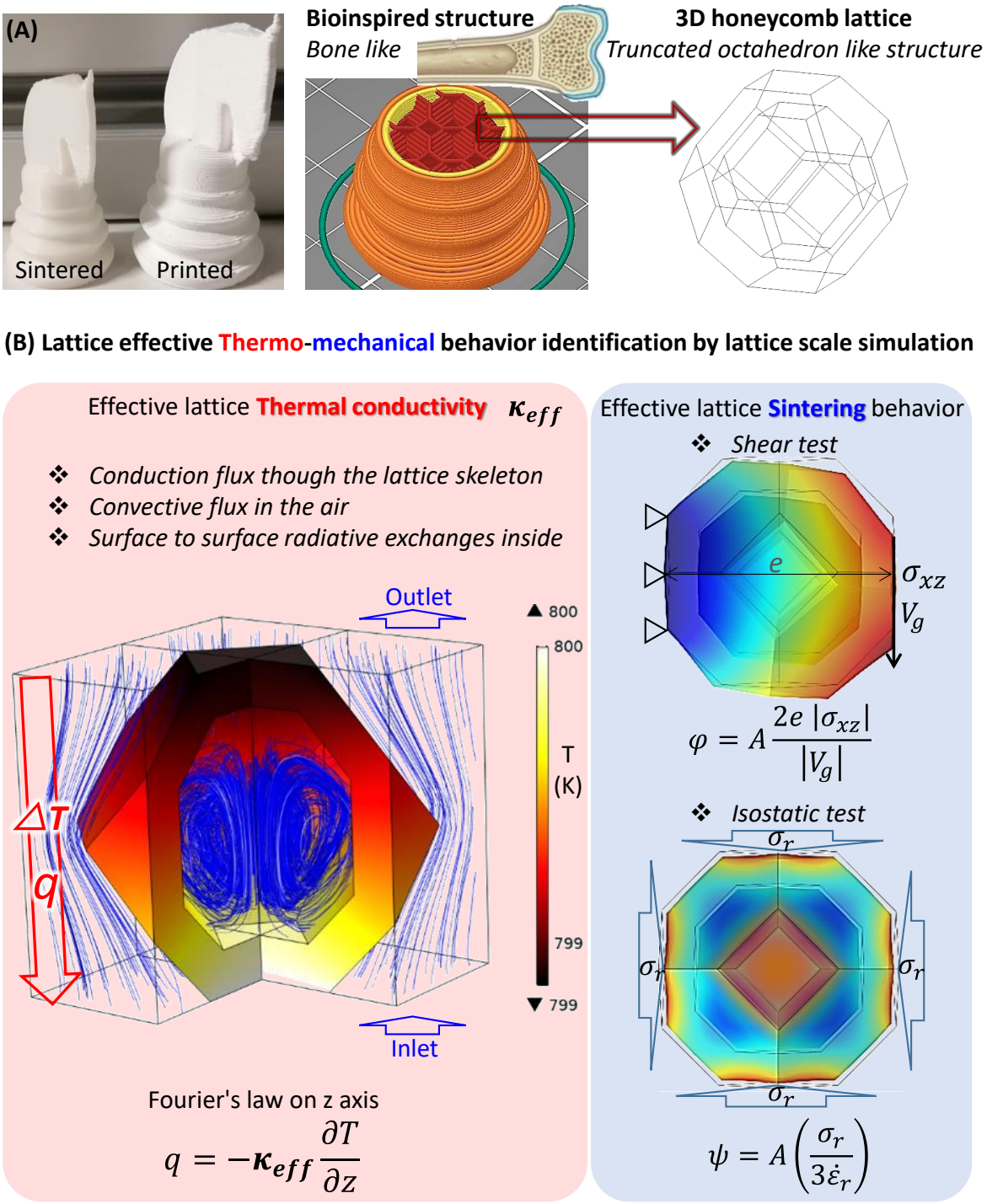

Figure 1 Identification of lattice thermomechanical behavior; (a) printed and sintered shape with internal honeycomb lattices based on truncated octahedron structure; (b) lattice scale simulation to identify the effective lattice thermal conductivity (left) and sintering behavior (right).

2.8.1. Thermal behavior.

The lattice scale thermal simulation has the objective of reproducing all heat transfer mechanisms in the lattices to determine their effective thermal conductivity. The lattice skeleton

is tested at different levels of densification and temperature. The heat transfer encompasses the conduction in the lattice skeleton, the surface to surface radiation between the lattices skeleton surfaces and the air convection inside the cavity. Such simulation can be done with the heat transfer module of COMSOL Multiphysics®. The conductivity of the porous skeleton is taken using the zirconia properties and the effective medium approximation formula (1-1.5Θ) to account for the porosity effect on the conductivity [55]. In order to measure the effective thermal conductivity, a heat flux is imposed on the upper and lower faces and the lateral faces used a symmetry condition (see figure 1b). The imposed heat flux (q) makes the development of a temperature difference on the Z axis ($\triangle T$) that is measured by a virtual probe to determine the effective thermal conductivity (κ_{eff}) by the following Fourier's relation[40,62].

$$q = -\kappa_{eff}\frac{\partial T}{\partial z} \tag{24}$$

The collected effective lattice thermal conductivity data are then fitted by a polynomial function for an easy implementation in the thermomechanical simulation.

2.8.2. Shear tests.

For the virtual shear tests, the configuration (reported in figure 1b) consists of the shear solicitation of the truncated octahedron structure. One side has a fixed constraint and the shear pressure is loaded on the opposite face. A virtual probe is located on this face to record the shear strain rate. These shear tests are made at different lattice skeleton porosity. The identification equation of the shear modulus is described below. Equation (8) can be simplified for a shear solicitation where the stress and strain rate tensors are reduced as follows.

$$\underline{\dot{\varepsilon}} \equiv \begin{pmatrix} 0 & 0 & \dot{\varepsilon}_{xz} \\ 0 & 0 & 0 \\ \dot{\varepsilon}_{xz} & 0 & 0 \end{pmatrix} \quad \underline{\sigma} \equiv \begin{pmatrix} 0 & 0 & \sigma_{xz} \\ 0 & 0 & 0 \\ \sigma_{xz} & 0 & 0 \end{pmatrix} \tag{25}$$

With the expression of the deviatoric stress tensor,

$$\underline{s} = \underline{\sigma} - \frac{I_1 \mathbb{1}}{3} = \underline{\sigma} \tag{26}$$

and the expression of the shear strain rate tensor,

$$|\dot{\varepsilon}_{xz}| = \frac{|V_g|}{2e} \tag{27}$$

the analytic formulation of the shear test becomes.

$$|\dot{\varepsilon}_{xz}| = \frac{|V_g|}{2e} = \frac{|\sigma_{xz}|}{2\eta\varphi_{eff}} \tag{28}$$

Consequently, the shear modulus can be identified by the virtual shear test using the following identification equation.

$$\varphi_{eff} = \frac{|\sigma_{xz}|}{(2\eta)|\dot{\varepsilon}_{xz}|} = \frac{2e\,|\sigma_{xz}|}{(2\eta)|V_g|} \tag{29}$$

With (2η), the viscosity expression described in equation (4).

2.8.3. Hydrostatic test.

The virtual hydrostatic test configuration is reported in figure 1b. The hydrostatic stress is applied on the external truncated octahedron surfaces and a virtual probe record the hydrostatic strain rate. Like for the shear test, different porosity tests are made to determine the bulk modulus. The identification equation considers the following hydrostatic simplifications for the stress, strain rate tensors and the deviatoric stress tensor.

$$\underline{\dot{\varepsilon}} \equiv \begin{pmatrix} \dot{\varepsilon}_r & 0 & 0 \\ 0 & \dot{\varepsilon}_r & 0 \\ 0 & 0 & \dot{\varepsilon}_r \end{pmatrix} \quad \underline{\sigma} \equiv \begin{pmatrix} \sigma_r & 0 & 0 \\ 0 & \sigma_r & 0 \\ 0 & 0 & \sigma_r \end{pmatrix} \quad \underline{s} = \underline{\sigma} - I_1 \mathbb{i}/3 = 0 \tag{30}$$

Rearranging (30) in (8), we obtain the following analytical model of the virtual hydrostatic test.

$$\dot{\varepsilon}_r = \frac{\sigma_r}{(2\eta)3\psi_{eff}} \tag{31}$$

The bulk modulus identification equation is as follows.

$$\psi_{eff} = \frac{\sigma_r}{(2\eta)3\dot{\varepsilon}_r} \tag{32}$$

3. Experiment and method

The 3D printing of porous zirconia green shape has been done by extrusion filament method with the commercial 1.75 mm filament called “White Zirconia Zetamix Filament” by nanoe®. The 3D printed sample can be debinded in two stages. A first step consists in a solvent

debinding of 6 hours in acetone at 40°C. After drying, the second debinding step consists in a thermal debinding in a furnace in air at 8 K/h up to 500°C. To preconsolidate the samples, a presintering step follows the debinding with a 3 K/min ramp up to 1000°C. The sintering cycle consists in a heating ramp of 3k/min to 1500°C. To determine the printed zirconia sintering behavior, 10 6×6×6 mm^3 cubes have been printed debinded and preconsolidate. The electron microscopy (SEM Jeol 7200 LV) was used to analyze the powder and sintered parts microstructures. The relative densities were determined by Archimedes' method. Sintering curves were measured on a Setaram® TMA96 dilatometer in four main steps.

i. In the first step, three constant heating rates to 1500°C of 1, 3 and 10K/min were done to determine the sintering activation energy by the master sintering curve and kinetic field method (see section 2.3).

ii. The direct regression calibration method described in section 2.3 is then used to determine the viscosity and calibrate the moduli in intermediate stages. The regression equation (16) is used with the modified moduli (17) and (18) in the intermediate sintering stage.

iii. To determine the final stage grain growth curves (still from the dilatometry curve), the method depicted in section 2.5 is used.

iv. Finally, the sintering anisotropy is introduced to model the shrinkage curves by using the sintering stress corrective equation (20) and adjusting the *c, c',c''* coefficients. The analytic sintering modeling has been done by an ordinary differential resolution on Octave-Forge software.

At this stage, the identified model can simulate the anisotropic sintering of 3D printed shapes if no lattice filling is used. To determine the thermomechanical behavior of 3D honeycomb lattice, the lattice scale simulation depicted in section 2.7 is used for different porosities. The effective moduli (φ_{eff}, ψ_{eff}) and thermal conductivity (κ_{eff}) are then used in the filling zone to simulate the lattice fragile behavior and low thermal conductivity. In this simulation, we

choose to compute the simulated relative density of the shell and the lattice zone as a same parameter. This implicates the computed porosity of lattice zone is in fact the porosity value of the lattice skeleton. This approach is interesting because it does not imply unstable abrupt transition in the porosity at the shell/lattice interface. However, because the effective lattice moduli are significantly lower in value than the shell, this would accelerate the sintering and de-synchronize the sintering between the lattice and the shell. Consequently, the sintering stress (P_l) in lattice need to exclude the macro-porosity between the skeleton. The porosity considered in equation (2) is then not the skeleton porosity but the total lattice porosity. The total relative density (D_{tot}) can be calculated from the filling density (D_{fill}) and the skeleton relative density ($D_{skeleton}$) by $D_{tot}=D_{skeleton}D_{fill}$. Actually, an adjustment of the apparent porosity used in P_l can be done to synchronize the lattice/shell densification. To illustrate such simulation that includes the lattice filling by effective parameters a knight-chess shape has been printed, sintered (see figure a) and simulated. An explorative simulation on bigger cylindrical shape and variable shell thickness and heating rate has been investigated to detect the kind of defects this simulation approach can anticipate.

4. Results and discussions

In this section, the four-stage identification of the anisotropic sintering behavior is first presented followed by the lattice effective moduli and thermal conductivity. Finally, the shell/lattice simulation of 3D printed shaped is presented through a knight-chess shape and by scalability stability simulations.

4.1. Zirconia powder analysis and sintering activation energy assessment.

In order to analyze the starting zirconia powder grain size distribution. A small piece of filament has been debinded chemically and thermally. The resulting powder has been analyzed by SEM and their grains sizes determined by the software ImageJ. The result is reported in figure 2a.

The starting powder has an average grain size of 105 nm and a grain size distribution from 40 nm to 240 nm. The 6 mm cubes were sintered at different heating rates by dilatometry. The sintering curves are reported in figure 2b. The densification temperatures range is between 1100°C and 1500°C. The different heating rates are shifted toward about 50K lower temperatures for each successive lower heating rate. These sintering curves are used in the next analysis to calculate the apparent sintering activation energy by the master sintering curve and kinetic field methods (step 1 in the identification method). The result of the master sintering curve is reported in figure 3a with on the upper graph, the master sintering curves at optimal activation energy and below, the minimization graph. The sintering activation energy is 650 kJ/mol. This value is in good agreement with the literature activation energies for 3Y mol% zirconia nano-powders with 625 kJ/mol obtained for the Tosoh® TZ-3Y-BE[27], the 667 kJ/mol obtained for 3Ymol% zirconia obtained by co-precipitation method [63], the 683 kJ/mol obtained for the Tosoh® TZ-3Y[64] or 647 kJ/mol for the same powder[65]. For comparison, the activation energy was also tested by the kinetic field method[24], the result is reported in figure 3b. A close value of 670 kJ/mol is obtained. This method shows that the activation energy is stable in the intermediate stage-sintering domain. Between the two methods, the activation energy of the master sintering curve is chosen for the next step as it is based on a global evaluation on the intermediate stage, the kinetic field value that is evaluated on each fixed porosity can be more easily sensitive to local errors in the sintering curves.

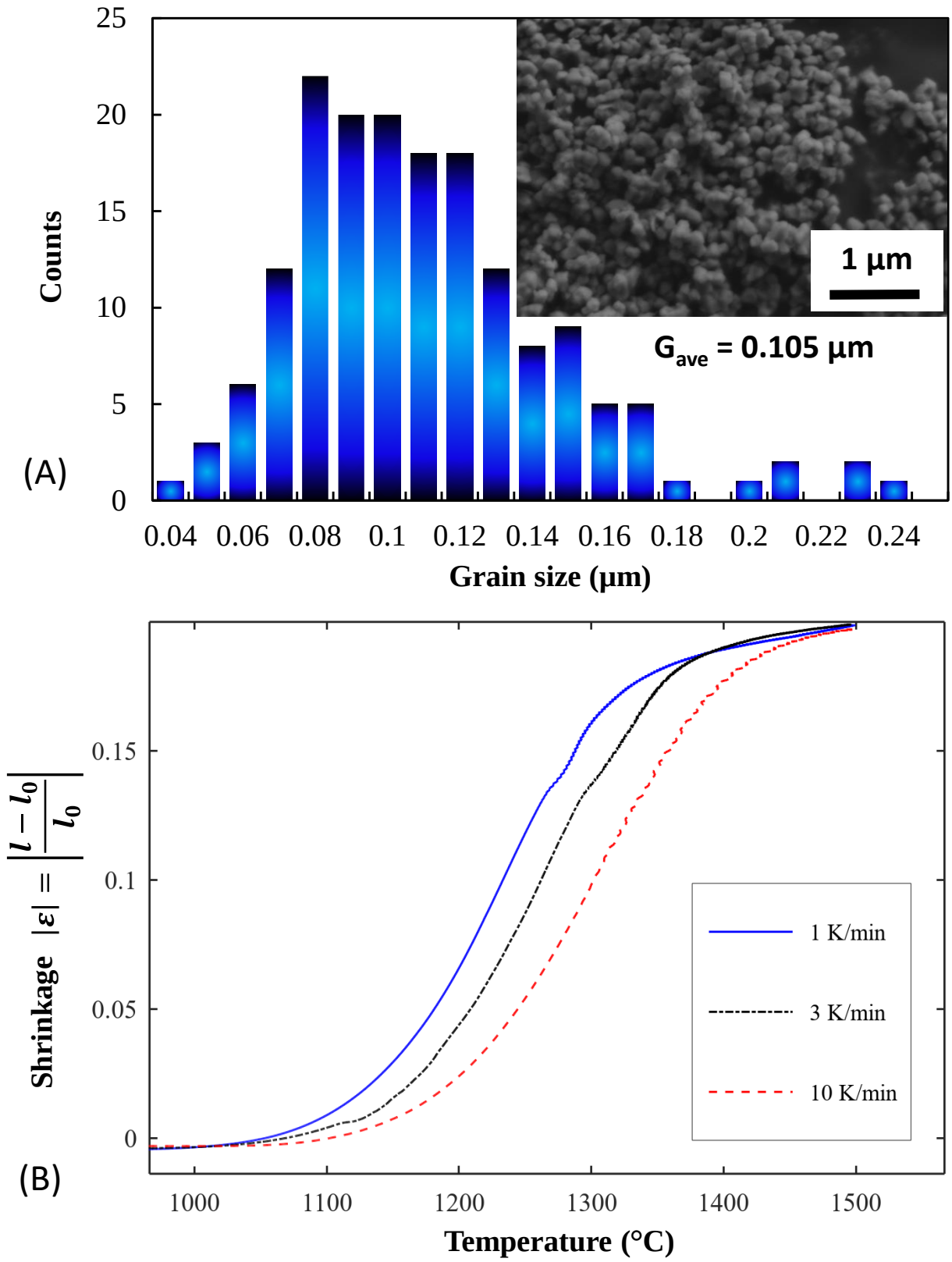

Figure 2 (a) Granulometry analysis on the debinded zetamix® zirconia filament, (b) constant heating rate dilatometry of the debinded, presintered 6 mm cubes for three heating rates.

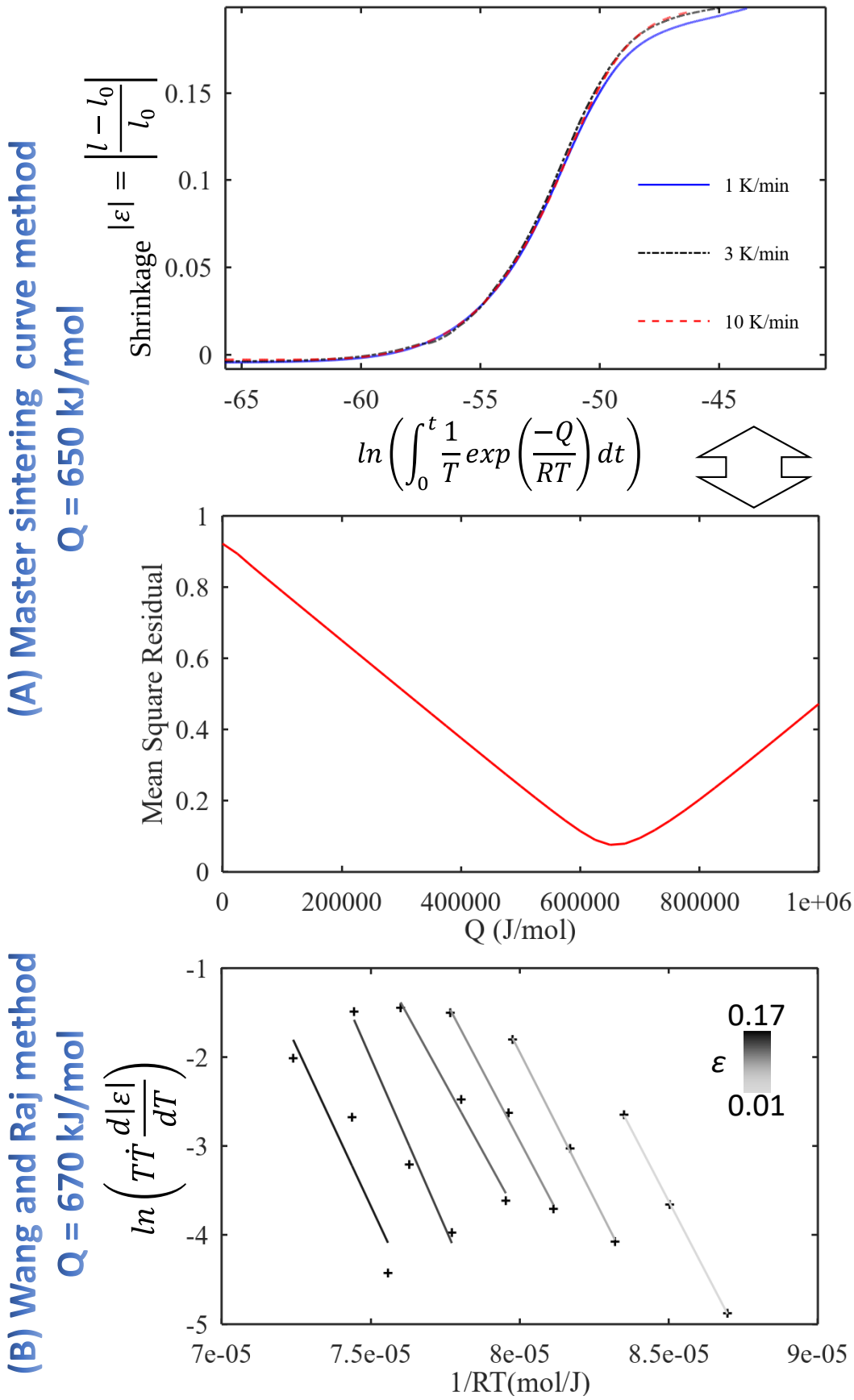

Figure 3 Sintering activation energy assessment by, (a) the mastering sintering curve and (b) the kinetic field method.

4.2. Identification of viscosity, moduli terms and final stage grain growth.

Now the sintering activation energy is independently determined, the next step of the identification process consists in plotting the linear regression equation (16) Y *vs* 1/RT. The surface energy of $\alpha = 1.37\ \mathrm{Jm}^{-2}$ as been used for zirconia[66]. In the beginning Skorohod's theoretical moduli equations (5), (6) are used and the activation energy of the slope of this regression gives a value much lower than the MSC value of 650 kJ/mol. It is at this stage that we replace the moduli by the modified Skorohod's moduli equations (17), (18) to adjust the initial critical porosity term (θ_{ci}). Generally, the modification of this unique parameter is enough to obtain a perfect linearization to the model in all intermediate stage sintering that reproduce a slope corresponding to the MSC moduli independent value. This corrected regression curve is reported in figure 2a. On the left, the θ_{ci} adjustment analysis is reported for each iteration, the absolute error of the regression slope with the MSC activation energy. The regression gives then a coherent value with MSC for a critical initial porosity of 0.5685. No other moduli constants or exponent have been modified for the linearization curve which is perfect with $\theta_{ci} = 0.5685$. In some cases, the other constants a, γ and ζ may also be modified from Skorohod's moduli [28,51,67]. However, this is rare because Skorohod's moduli is adapted to final stage sintering, with the initial stage correction by θ_{ci}, the whole moduli curve is generally corrected. With the modified moduli, the viscosity pre-exponential constant can be determined from the origin of the regression curve. The value $\eta_0 = 2.6E-13\ PasK^{-1}$ is obtained.

Once the viscosity and moduli terms are identified, the next step is to identify the final stage sintering grain growth. The method uses equation (19) where all unknown parameters are determined. With the final stage porosity elimination curve ($\dot{\theta}$) that can be obtained from the dilatometry[27]. Two grain growth curves can be plotted (see figure 4b) for the lattice (m=2) and grain boundary diffusion (m=3) hypothesis. At this stage, it is very important to consider the final critical porosity term θ_{cf} in the bulk modulus because the principle of the method is

the estimate the grain growth curve by the densification rate decrease at the final stage to grain growth[27]. If the 3D printing macroporosity is not corrected in the bulk modulus, an excessive grain growth will be predicted by equation (19) to compensate for the low-final stage apparent relative densities. A coherent value of $\theta_{cf} = 0.03$ is determined. With this last correction, the predicted grain size curves of figure 4b were obtained. The experimental value of final grain size indicates clearly a grain boundary diffusion mechanism. With the obtained grain size curve, the grain growth model is identified using equation (9) and p=2 [27,68]. The result linear regression is reported in figure 4b (right). The following parameters are identified $k_0 = 8.25E-5\ m^{1+p}s^{-1}$ and $Q_G = 624kJ/mol$. With these last parameters, the densification curves can be modeled, only the anisotropy behavior remains to be determined in the next section.

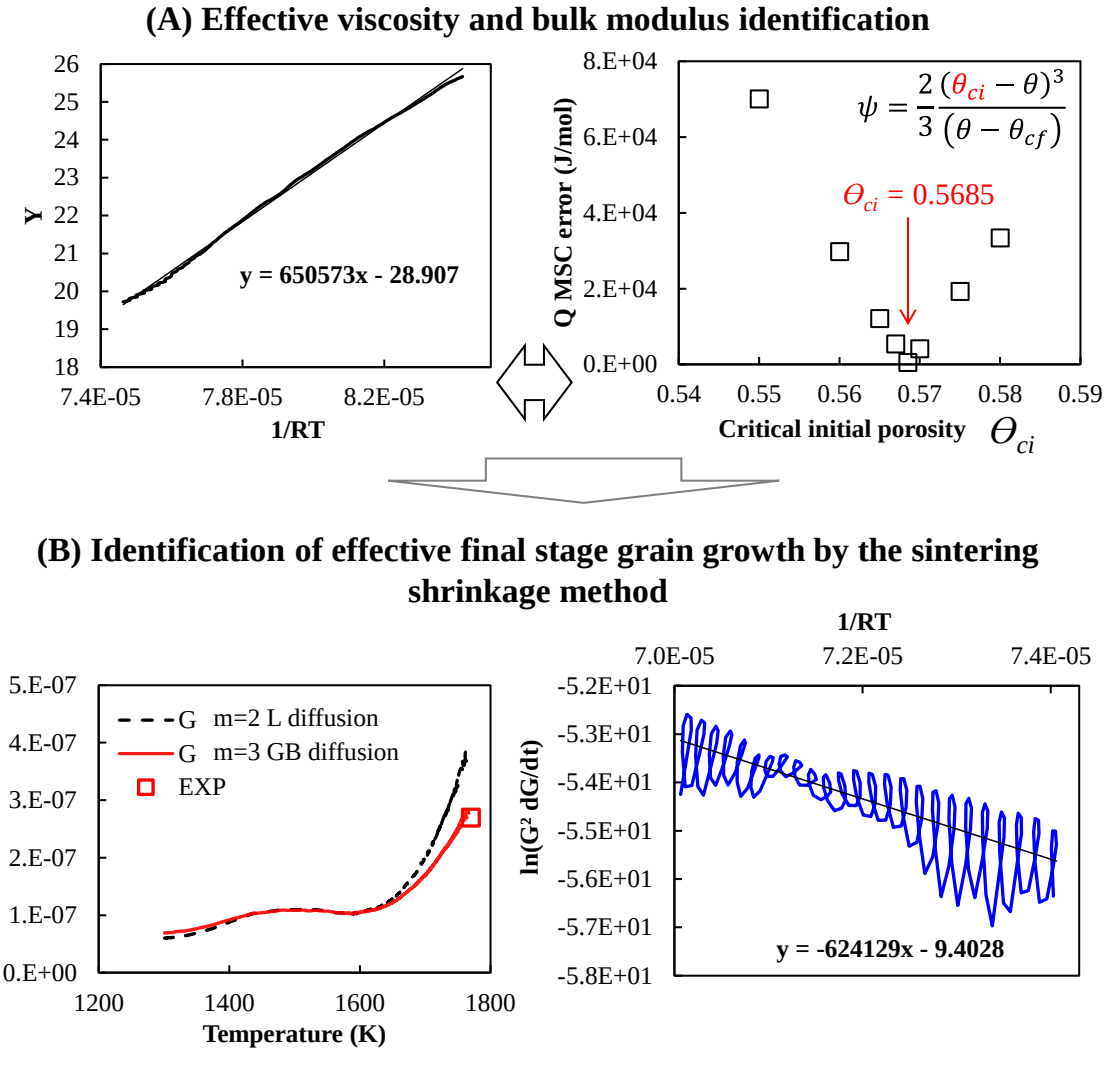

Figure 4 Sintering model identification, (a) viscosity, moduli, (b) final stage grain growth.

4.3. Sintering anisotropy.

The final stage of the identification process involves the modeling of sintering anisotropy. To achieve this, the P_l sintering stress expression, initially isotropic, is transformed into an anisotropic form through analytic modeling to better represent the anisotropy observed in the shrinkage curves. Equation (2) of the Pl model is subsequently replaced by Equation (20). The coefficients *c,c',c''* are adjusted to fit the dilatometry shrinkage curves. Special care is taken to reproduce the shrinkage curves without affecting the relative density curve. The resulting modeling curves and their respective experimental data are presented in Figure 5.

In Figure 5a, a comparison of the relative density curves is provided. This demonstrates that the modification for sintering anisotropy does not affect densification curves. The experimental and modeled shrinkage curves are reported in Figure 5b. A more significant shrinkage is observed in the building direction (Z-axis) compared to the two in-plane layer directions (R-axis). The anisotropic P_l term is as follows. No differences appear in the in-plane two directions (X, Y ≡ R) due to the printing strategy employing mixed in-plane orientation.

$$\begin{cases} P_{lz} = Pl\,(1 + \theta) \\ P_{lr} = Pl\,(1 + 0.7\theta) \end{cases} \tag{33}$$

The simulated grain growth curve is reported in figure 5c. The polished SEM microstructure is also reported with the identified average grain size of 270 nm. Like for the graph in figure 4b, the grain growth model is coherent with the final grain size. In figure5a, the final stage critical porosity of 3% is represented in the densification curves. The grain growth helps predict the final stage sintering densification curves while being in good agreement with the final grain size.

At this stage, the 3D printed/debinded zirconia sintering behavior is fully identified. The last aspect to be determined, which is the objective of this article, is to determine the thermo-mechanical behavior of the 3D honeycomb lattices.

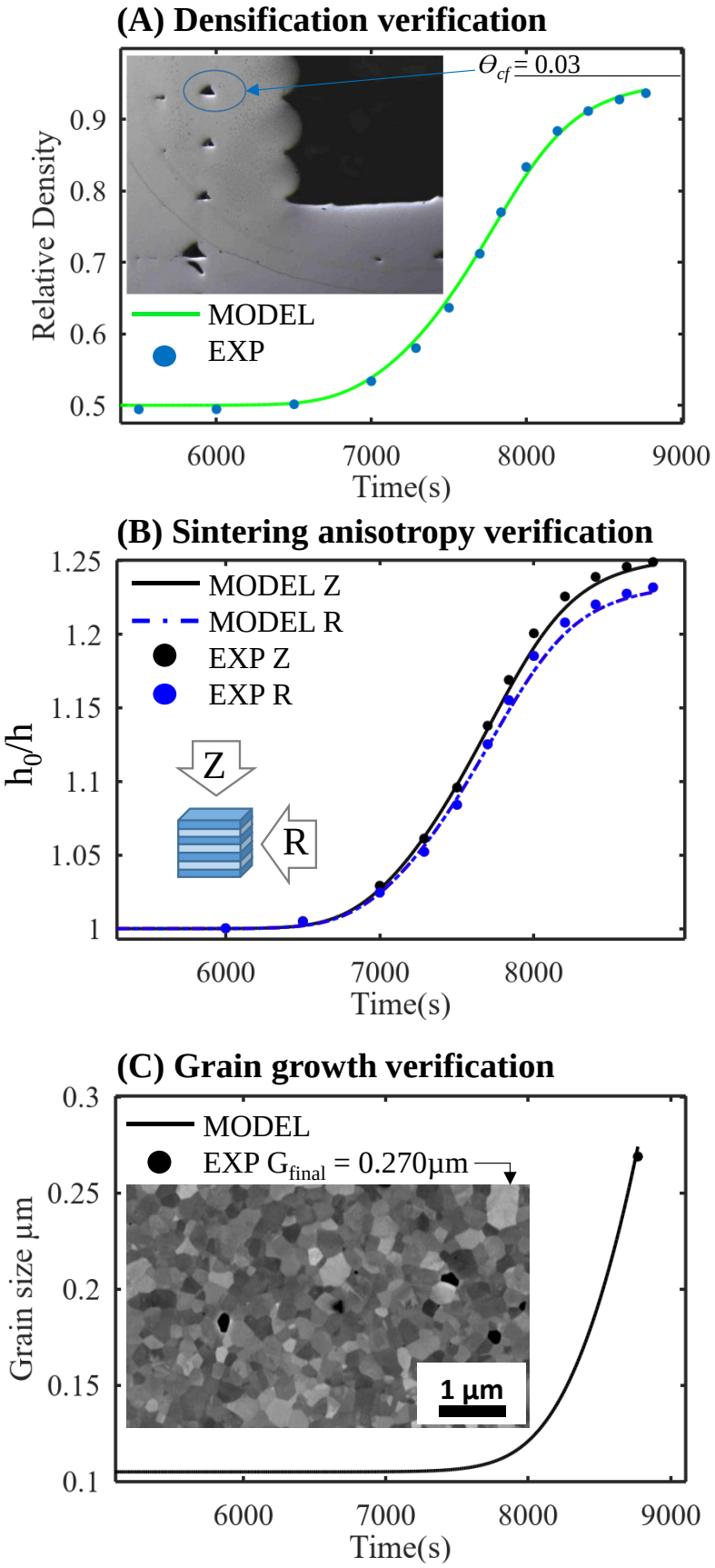

Figure 5 Identified anisotropic sintering model compared to experimental data, (a) densification, (b) shrinkage, (c) grain growth.

4.4. Lattice heat transfer behavior assessment.

In this simulation, the effective lattice geometry thermal conductivity is determined by simulating an imposed heat flux (q) across the lattice. The developed temperature difference ($\triangle T$) is measured, and the effective thermal conductivity (κ_{eff}) is determined by equation (24). A simulation image of the lattice temperature distribution is reported in figure 6a. The simulation shows by the blue line the convection developed in the open and closed lattice cavities. The color bar indicates the temperature in the porous lattice skeleton. The temperature in the air is calculated together with convection but not represented in this image. The radiative exchanges in lattice cavities are also modeled using 0.7 for the emissivity of zirconia [69]. The heat transfer simulation is tested for temperature and skeleton relative density ranges of 300-1700K and 0.5-1, respectively. The lattice effective thermal conductivity surface response is plotted in figure 6b, the polynomial fitting of this surface response in W/(mK) unit is also reported in the figure.

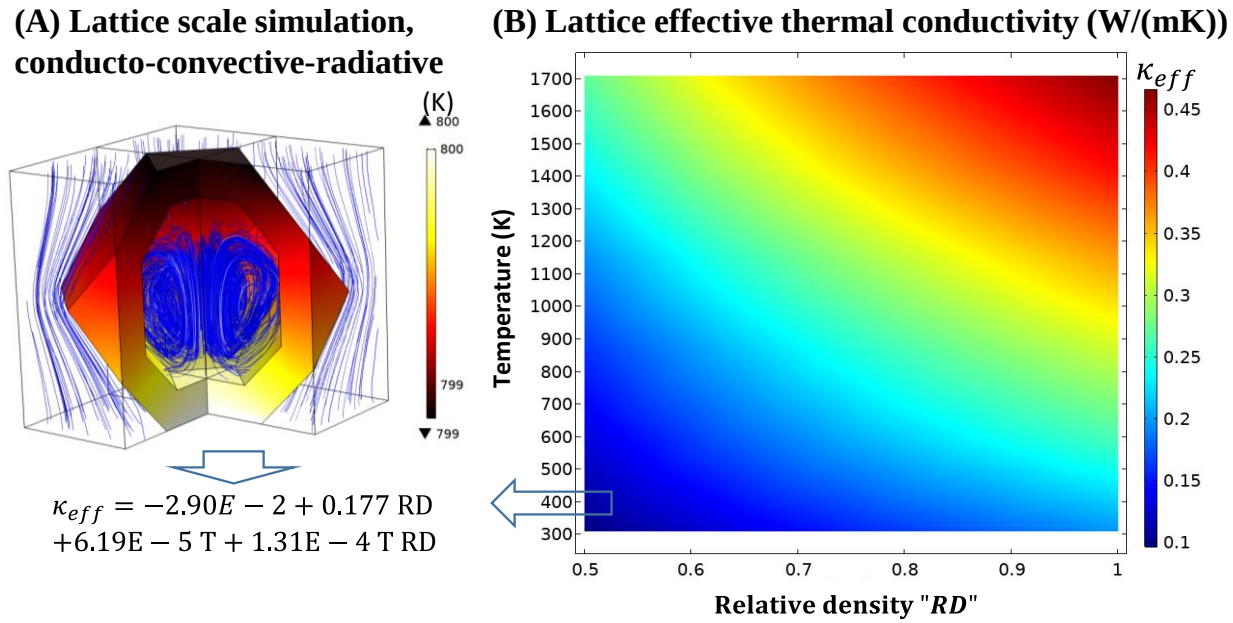

Figure 6 Lattice thermal behavior identification, (a) simulation image of the conductive-convective-radiative model, (b) surface response of the lattice effective conductivity data.

4.5. Effective lattice sintering behavior assessment.

As presented is sections 2.7.2 and 2.7.3, shear and hydrostatic stress are applied to the 3D honeycomb lattice to determine the shear and bulk moduli by equations (29) and (32), respectively. The identified effective moduli data points are reported in figure 7. Compared to the moduli values for the lattice skeleton (dashed curves), the high void in the lattice cavities implies a significantly more deformable behavior with effective lattice moduli values 10 to 50× lower than their constitutive porous skeleton material. These very low moduli will enable the simulation of the fragile lattice sintering behavior. The moduli data points have been mathematically fitted (see equations in figure 7) for an easy implementation in the finite element code. One important aspect is the fact that the effective shear modulus does not tend to 1 for the lattice skeleton relative density of 1. This simulates the fact that voids within lattice cavities remain even when the lattice skeleton sintering is finished. This helps simulate the highly deformable behavior of the lattice at high temperatures compared to the fully dense printing filling strategy. For the effective bulk modulus, the identified data points behave in the same way and for a skeleton relative density of 1, the lattice moduli do not tend to infinite like for the skeleton. In this precise case, the sintering must stop when the lattice skeleton sintering is finished. Consequently, the same final critical porosity of 3% has been introduced in the fitting equation to force the end of lattice sintering when the skeleton sintering is finished at 3%. The effective modulus tends to infinite but only after 90%. Compared to the skeleton moduli, the lattice bulk modulus still models the highly deformable behavior in hydrostatic solicitations.

At this stage, both the printed structure (shell) and lattice sintering behaviors are identified. The simulation of real printed ceramics with internal lattices is possible and depicted in the following section.

(A) Shear test: lattice effective shear modulus identification

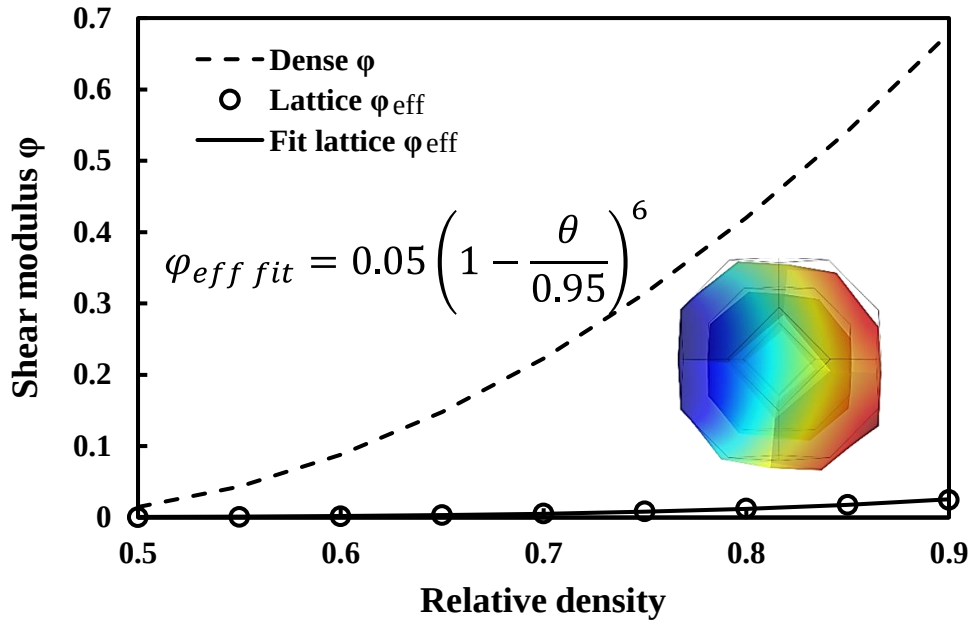

(B) Isostatic test: lattice effective bulk modulus identification

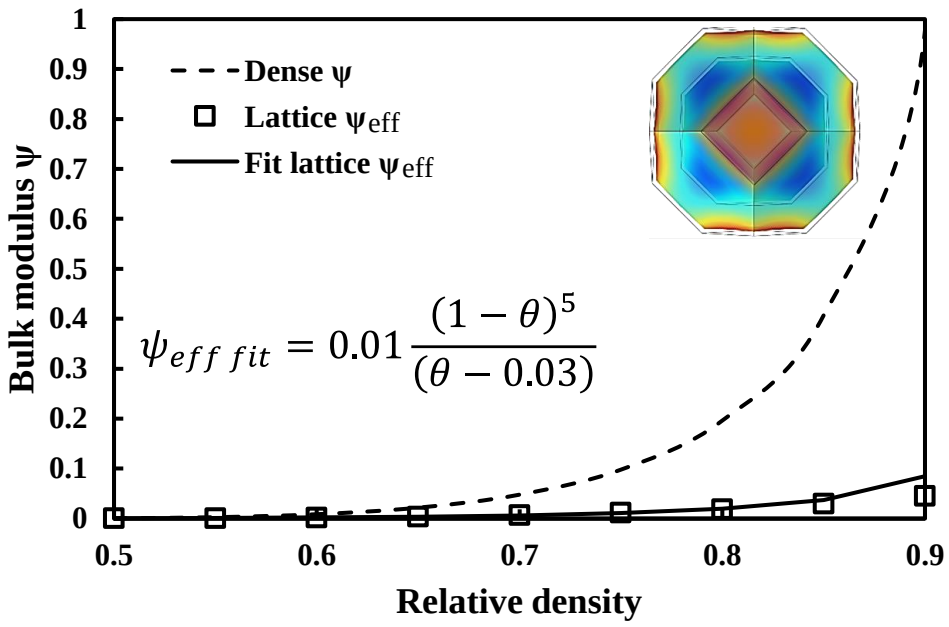

Figure 7 Identification of the lattice effective moduli by, (a) shear lattice tests, and (b) hydrostatic tests; the "dense" mention in the legend refers to the printed zirconia structure (shell) as opposed to the "lattice" that has cavity void.

4.6. Simulation of a zirconia 3D printed knight-chess shapes with shell/lattice zones.

The thermomechanical sintering of a 3D printed ceramic shape is possible if the identified viscosity, moduli, and porous zirconia thermal conductivity parameters are used in the external shell and the effective lattice moduli and thermal conductivity are used in the inner lattice zone. These two zones are represented in figure 8 with in red the lattice zones. On the right, the average relative density curves in the shell (blue) and lattice (green) are presented. As it can be observed, after taking into account the filling density (D_{fill}) for the lattice sintering stress, the two sintering curves are very close despite their very different moduli. The lower thermal conductivities identified imply the development of a center/edge thermal gradients with about 10 K of temperature difference during the heating. Knowing the height of the knight-chess shapes is 43 mm and the base diameter is 22 mm, this temperature difference looks reasonable. The shell that is directly exposed to the furnace temperature is then subjected to the faster heating, which could explain the slight advance of the shell densification curve. The difference can be seen in the relative density evolution in the shape during the heating (figure 8). The calculation of such 3D printed shapes was stable and takes about 20 minutes, showing the high potential of such an approach to test the sintering feasibility of different printing strategies.

However, the knight-chess shape is a laboratory-scale test, and one of the main interests of such simulations is to investigate the sintering behavior of bigger shapes. To test this aspect virtually, we have established in the next section a 2Daxisymmetric simulation that is even faster and takes a few minutes to estimate the scalability and heating issues.

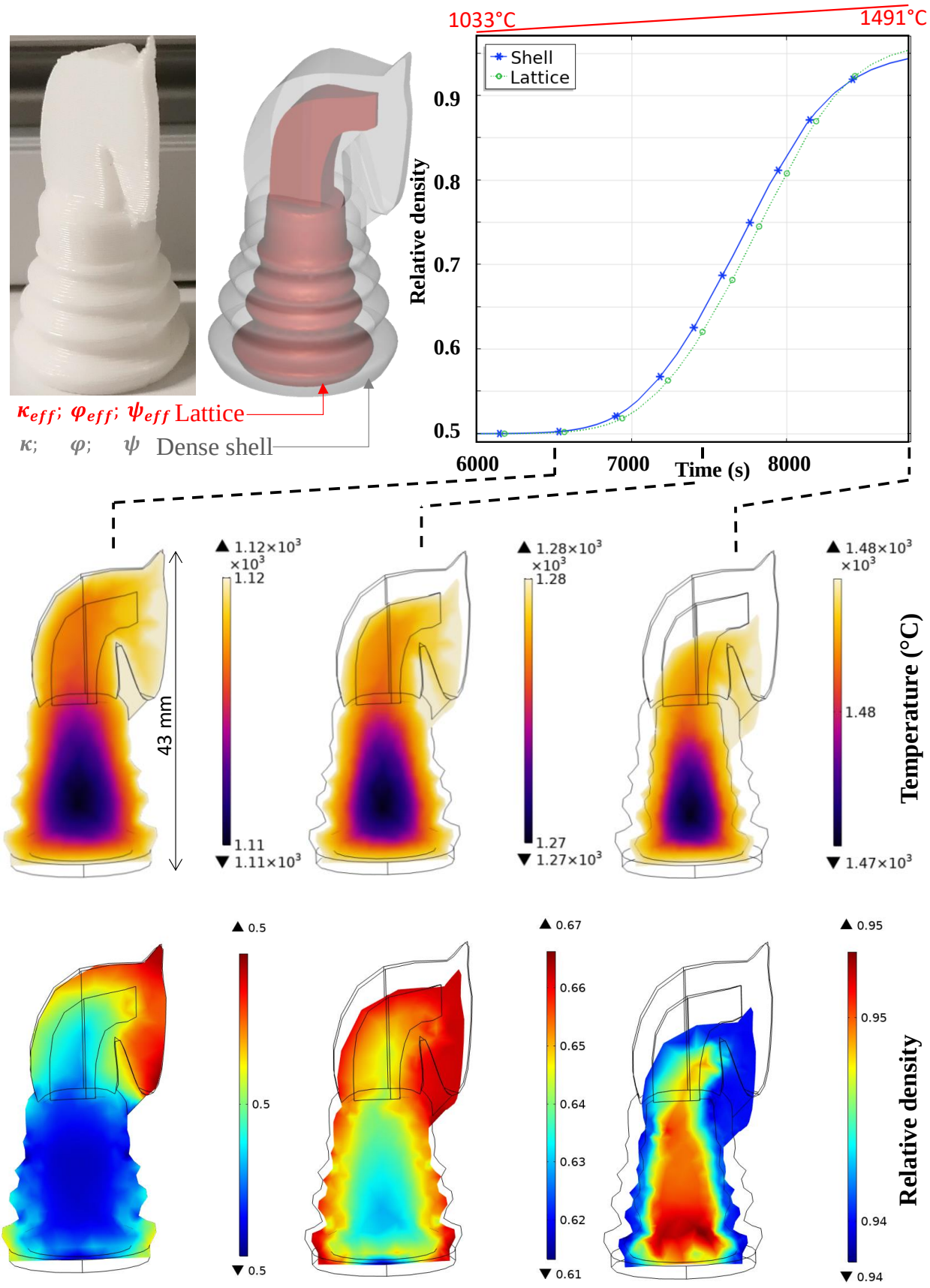

Figure 8 Simulation of the knight-chess printed part including the shell and lattices zone (red), the average densification curves of the shell and lattices are reported with simulation image captures at different stages of the sintering.

4.7. 2D axisymmetric simulation of parametric stability and scalability analysis.

The 2D axisymmetric model is reported in figure 9a and considers a regular cylindrical shape with 60 mm in diameter and 60 mm in height to represent a larger 3D printed object. For the lattices zone, a variable shell thickness is added on the external lattice zone surfaces. Like for the previous simulation, the temperature of the cycle is imposed at the external surface of the shell, and κ_{eff}, φ_{eff}, ψ_{eff} are considered in the lattices zone. An example of simulation capture of a 2 mm thick shell with a heating rate of 20 K/min is reported in figure 9b. This simulation represents the selected time where the distortion is maximum. We can clearly see that on bigger shapes, the developed temperature difference can be increased up to 40 K. This is explained by the higher time required for the heat to diffuse inside the core of the shape from the external surface. The consequence of this is a stronger delay in the sintering of the lattices (colder), which puts the external shell in severe tension of about 10 MPa. Distortions result from this shell stress. In reality, such conditions can generate cracks on the shell or in the internal lattice network.

The parametric virtual exploration has tested the shell thicknesses from 1 to 5 mm and the heating rate from 10 to 50K/min. The result of stability maps are reported in figure 9c. The first graph reports the maximum cycle shell distortion, which is calculated by the planar error sum of horizontal and vertical shells. The other graph reports the maximum cycle von Mises stress at Gauss points. This helps represent stability maps that can be used to predict if a printed shape has critical thickness zones that could require a slower heating rate or smaller different thickness. The distortions map indicate the stability zones for the lower heating rate and thicker shell. A thicker shell makes it less sensitive to distortions. The stress map gives similar results, but it is interesting to see that the stress developed does not correspond to the maximum distortions profiles except in extreme zones. Indeed, high distortion can relax the developed stress, and the simulation is highly sensitive to local stress intensification. The more reliable information is then the distortions map, which is precisely the parameter to minimize.

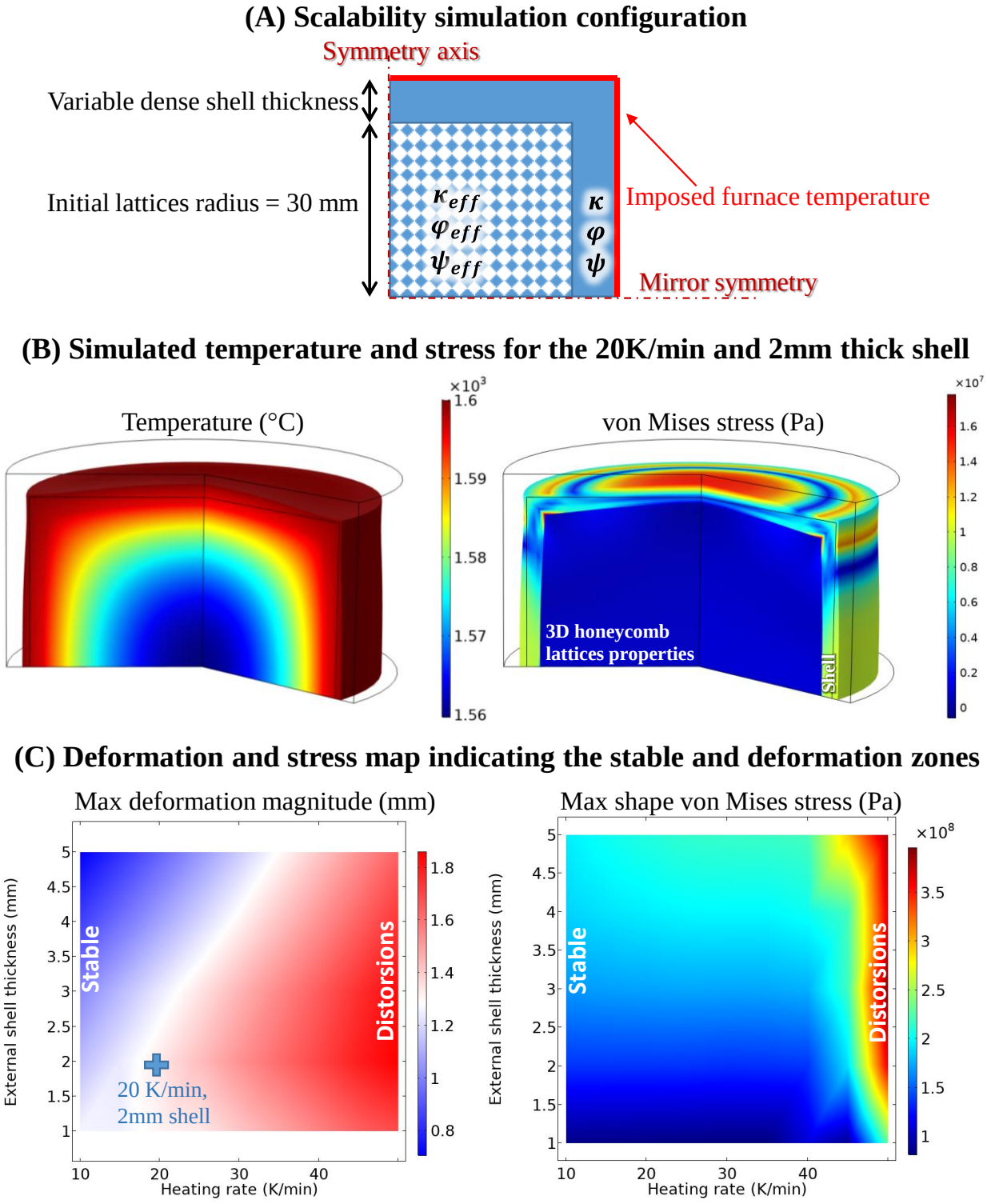

Figure 9 Parametric investigation of heating rate and shell thickness sintering stability; (a) simulation configuration, (b) example of simulation capture, (c) maximum cycle distortions and stress stability maps.

5. Conclusion

The main objective of this study was to propose a solution to robustly simulate 3D printed shapes containing complex internal lattice networks. The method proposed consists of simulating the lattice zones not by the lattice's real geometry, which would be unstable and highly time-consuming, but by an effective continuous compressible medium that reproduces the lattice's thermomechanical behavior. A specific identification method has been developed for the assessment of the 3D printed anisotropic sintering behavior and lattice-scale simulations to determine the lattice's effective sintering behavior and the lower thermal conductivity. The sintering model determination is based on dilatometry and includes four steps. The first step identifies the activation energy by the master sintering curve model; this value is combined with a regression approach to determine the viscosity and calibrate the moduli. The final stage sintering dilatometry curve is used to determine the grain growth behavior by an inversion method. Finally, the anisotropy is implemented *via* the sintering stress. The lattice moduli are determined by shear and hydrostatic virtual tests. Their values are very low and permit simulating the high deformability of inner lattice in 3D printed shapes.

The resulting simulation incorporates the lattice/shell behaviors. It is very stable and takes only a fraction of the sintering time, which is particularly interesting for conducting optimization analysis. An even faster 2D axisymmetric model has been implemented to run stability map parametric simulations, which identifies severe distortion conditions. This tool can be used to quickly estimate if a complex shape designed to be printed has thick zones that may not resist the sintering cycle. The latter can be used to adjust the heating rate and the shell thickness of the part to be 3D printed and sintered.

Acknowledgements

The help and support of Jérôme Lecourt and Christelle Bilot are gratefully acknowledged.

References

[1] A. Velasco-Hogan, J. Xu, M.A. Meyers, Additive Manufacturing as a Method to Design and Optimize Bioinspired Structures, Adv. Mater. 30 (2018) 1800940. https://doi.org/10.1002/adma.201800940.

[2] Q. Zhang, X. Yang, P. Li, G. Huang, S. Feng, C. Shen, B. Han, X. Zhang, F. Jin, F. Xu, T.J. Lu, Bioinspired engineering of honeycomb structure – Using nature to inspire human innovation, Prog. Mater. Sci. 74 (2015) 332–400. https://doi.org/10.1016/j.pmatsci.2015.05.001.

[3] E. Feilden, C. Ferraro, Q. Zhang, E. García-Tuñón, E. D'Elia, F. Giuliani, L. Vandeperre, E. Saiz, 3D Printing Bioinspired Ceramic Composites, Sci. Rep. 7 (2017) 13759. https://doi.org/10.1038/s41598-017-14236-9.

[4] Y. Lakhdar, C. Tuck, J. Binner, A. Terry, R. Goodridge, Additive manufacturing of advanced ceramic materials, Prog. Mater. Sci. 116 (2021) 100736. https://doi.org/10.1016/j.pmatsci.2020.100736.

[5] Y. Yang, X. Song, X. Li, Z. Chen, C. Zhou, Q. Zhou, Y. Chen, Recent Progress in Biomimetic Additive Manufacturing Technology: From Materials to Functional Structures, Adv. Mater. 30 (2018) 1706539. https://doi.org/10.1002/adma.201706539.

[6] A. du Plessis, C. Broeckhoven, I. Yadroitsava, I. Yadroitsev, C.H. Hands, R. Kunju, D. Bhate, Beautiful and Functional: A Review of Biomimetic Design in Additive Manufacturing, Addit. Manuf. 27 (2019) 408–427. https://doi.org/10.1016/j.addma.2019.03.033.

[7] J. Zhu, H. Zhou, C. Wang, L. Zhou, S. Yuan, W. Zhang, A review of topology optimization for additive manufacturing: Status and challenges, Chinese J. Aeronaut. 34 (2021) 91–110. https://doi.org/10.1016/j.cja.2020.09.020.

[8] Z. Li, Z. Chen, J. Liu, Y. Fu, C. Liu, P. Wang, M. Jiang, C. Lao, Additive manufacturing of lightweight and high-strength polymer-derived SiOC ceramics, Virtual Phys. Prototyp. 15 (2020) 163–177. https://doi.org/10.1080/17452759.2019.1710919.

[9] M. Orme, I. Madera, M. Gschweitl, M. Ferrari, Topology Optimization for Additive Manufacturing as an Enabler for Light Weight Flight Hardware, Designs. 2 (2018) 51. https://doi.org/10.3390/designs2040051.

[10] D.S. Nguyen, Design of lattice structure for additive manufacturing in CAD environment, J. Adv. Mech. Des. Syst. Manuf. 13 (2019) JAMDSM0057–JAMDSM0057. https://doi.org/10.1299/jamdsm.2019jamdsm0057.

[11] T. Chartier, A. Badev, Rapid Prototyping of Ceramics, in: Handb. Adv. Ceram., Elsevier, 2013: pp. 489–524. https://doi.org/10.1016/B978-0-12-385469-8.00028-9.

[12] T. Ohji, Additive manufacturing of ceramic components, Synthesiology. 11 (2018) 81–93. https://doi.org/10.5571/synth.11.2_81.

[13] J. Deckers, J. Vleugels, J.P. Kruth, Additive Manufacturing of Ceramics: A Review, J. Ceram. Sci. Technol. 5 (2014) 245–260. https://doi.org/10.4416/JCST2014-00032.

[14] Z. Chen, Z. Li, J. Li, C. Liu, C. Lao, Y. Fu, C. Liu, Y. Li, P. Wang, Y. He, 3D printing of ceramics: A review, J. Eur. Ceram. Soc. 39 (2019) 661–687. https://doi.org/10.1016/j.jeurceramsoc.2018.11.013.

[15] H. Li, L. Song, J. Sun, J. Ma, Z. Shen, Dental ceramic prostheses by stereolithography-based additive manufacturing: potentials and challenges, Adv. Appl. Ceram. 118 (2019) 30–36. https://doi.org/10.1080/17436753.2018.1447834.

[16] T. Yu, Z. Zhang, Q. Liu, R. Kuliiev, N. Orlovskaya, D. Wu, Extrusion-based additive manufacturing of yttria-partially-stabilized zirconia ceramics, Ceram. Int. 46 (2020) 5020–5027. https://doi.org/10.1016/j.ceramint.2019.10.245.

[17] J. Zhang, M. Yarahmadi, L. Cabezas, M. Serra, S. Elizalde, J.M. Cabrera, L. Llanes, G. Fargas, Robocasting of dense 8Y zirconia parts: Rheology, printing, and mechanical properties, J. Eur. Ceram. Soc. 43 (2023) 2794–2804. https://doi.org/10.1016/j.jeurceramsoc.2022.11.042.

[18] J. Jiang, X. Xu, J. Stringer, Support Structures for Additive Manufacturing: A Review, J. Manuf. Mater. Process. 2 (2018) 64. https://doi.org/10.3390/jmmp2040064.

[19] R.K. Bordia, S.-J.L. Kang, E.A. Olevsky, Current understanding and future research directions at the onset of the next century of sintering science and technology, J. Am. Ceram. Soc. 100 (2017) 2314–2352. https://doi.org/10.1111/jace.14919.

[20] E.A. Olevsky, Theory of sintering: from discrete to continuum, Mater. Sci. Eng. R Reports. 23 (1998) 41–100. https://doi.org/10.1016/S0927-796X(98)00009-6.

[21] V.V. Skorohod, Rheological basis of the theory of sintering, Nauk. Dumka, Kiev. (1972).

[22] H. Su, D.L. Johnson, Master Sintering Curve: A Practical Approach to Sintering, J. Am. Ceram. Soc. 79 (1996) 3211–3217. https://doi.org/10.1111/j.1151-2916.1996.tb08097.x.

[23] S.J. Park, P. Suri, E. Olevsky, R.M. German, Master Sintering Curve Formulated from Constitutive Models, J. Am. Ceram. Soc. 92 (2009) 1410–1413. https://doi.org/10.1111/j.1551-2916.2009.02983.x.

[24] J. Wang, R. Raj, Estimate of the Activation Energies for Boundary Diffusion from Rate-Controlled Sintering of Pure Alumina, and Alumina Doped with Zirconia or Titania, J. Am. Ceram. Soc. 73 (1990) 1172–1175. https://doi.org/10.1111/j.1151-2916.1990.tb05175.x.

[25] F. Raether, P. Schulze Horn, Investigation of sintering mechanisms of alumina using kinetic field and master sintering diagrams, J. Eur. Ceram. Soc. 29 (2009) 2225–2234. https://doi.org/10.1016/j.jeurceramsoc.2009.01.025.

[26] C. Manière, E. Saccardo, G. Lee, J. McKittrick, A. Molinari, E.A. Olevsky, Swelling negation during sintering of sterling silver: An experimental and theoretical approach, Results Phys. 11 (2018) 79–84. https://doi.org/10.1016/j.rinp.2018.08.035.
[27] C. Manière, T. Grippi, S. Marinel, Estimate microstructure development from sintering shrinkage: A kinetic field approach, Mater. Today Commun. 31 (2022) 103269. https://doi.org/10.1016/j.mtcomm.2022.103269.
[28] T. Grippi, S. Béhar-Lafenêtre, H. Friedrich, D. Haas, U. Schenderlein, S. Marinel, C. Manière, Densification modeling for gas pressure sintered silicon nitride-based ceramics with Thermo-Optical dilatometry, J. Eur. Ceram. Soc. 44 (2024) 822–830. https://doi.org/10.1016/j.jeurceramsoc.2023.09.028.
[29] C. Manière, G. Kerbart, C. Harnois, S. Marinel, Modeling sintering anisotropy in ceramic stereolithography of silica, Acta Mater. 182 (2020) 163–171. https://doi.org/10.1016/j.actamat.2019.10.032.
[30] Q. Li, W. Hou, J. Liang, C. Zhang, J. Li, Y. Zhou, X. Sun, Controlling the anisotropy behaviour of 3D printed ceramic cores: From intralayer particle distribution to interlayer pore evolution, Addit. Manuf. 58 (2022) 103055. https://doi.org/10.1016/j.addma.2022.103055.
[31] P. Kakanuru, K. Pochiraju, Simulation of shrinkage during sintering of additively manufactured silica green bodies, Addit. Manuf. 56 (2022) 102908. https://doi.org/10.1016/j.addma.2022.102908.
[32] C. Manière, C. Harnois, S. Marinel, 3D printing of porcelain: finite element simulation of anisotropic sintering, Int. J. Adv. Manuf. Technol. 116 (2021) 3263–3275. https://doi.org/10.1007/s00170-021-07304-y.
[33] L.-J. Wen, X.-G. Hu, Z. Li, Zhan-Hua Wang, J.-K. Wu, Q. Zhu, Anisotropy in tensile properties and fracture behaviour of 316L stainless steel parts manufactured by fused deposition modelling and sintering, Adv. Manuf. 10 (2022) 345–355. https://doi.org/10.1007/s40436-022-00402-4.
[34] A. Cabo Rios, E. Hryha, E. Olevsky, P. Harlin, Sintering anisotropy of binder jetted 316L stainless steel: part I – sintering anisotropy, Powder Metall. 65 (2022) 273–282. https://doi.org/10.1080/00325899.2021.2020485.
[35] M. Zago, N.F.M. Lecis, M. Vedani, I. Cristofolini, Dimensional and geometrical precision of parts produced by binder jetting process as affected by the anisotropic shrinkage on sintering, Addit. Manuf. 43 (2021) 102007. https://doi.org/10.1016/j.addma.2021.102007.
[36] C. Manière, C. Harnois, S. Marinel, Sintering behavior of ultra-thin 3D printed alumina lattice structures, Acta Mater. 250 (2023) 118865. https://doi.org/10.1016/j.actamat.2023.118865.
[37] R. Bordia, R. Zuo, O. Guillon, S. Salamone, J. Rodel, Anisotropic constitutive laws for sintering bodies, Acta Mater. 54 (2006) 111–118. https://doi.org/10.1016/j.actamat.2005.08.025.
[38] E. Olevsky, V. Skorohod, Deformation aspects of anisotropic-porous bodies sintering, Le J. Phys. IV. 03 (1993) C7-739-C7-742. https://doi.org/10.1051/jp4:19937117.
[39] B. Sarbandi, J. Besson, M. Boussuge, D. Ryckelynck, F. Barlat, Y.H. Moon, M.G. Lee, Anisotropic constitutive model and FE simulation of the sintering process of slip cast traditional porcelain, in: AIP Conf. Proc., 2010: pp. 689–696. https://doi.org/10.1063/1.3457622.
[40] L. Moreno-Sanabria, R. Barea, M.I. Osendi, M. Belmonte, P. Miranzo, Modelling the anisotropic thermal conductivity of 3D logpile structures, J. Eur. Ceram. Soc. 43 (2023) 4462–4471. https://doi.org/10.1016/j.jeurceramsoc.2023.03.017.
[41] D. Muñoz Codorníu, J.J. Moyano, M. Belmonte, M.I. Osendi, P. Miranzo, Thermal conduction in three-dimensional printed porous samples by high resolution infrared thermography, Open Ceram. 4 (2020) 100028. https://doi.org/10.1016/j.oceram.2020.100028.
[42] S. Bhandari, C. Manière, F. Sedona, E. De Bona, V.M. Sglavo, P. Colombo, L. Fambri, M. Biesuz, G. Franchin, Ultra-rapid debinding and sintering of additively manufactured ceramics by ultrafast high-temperature sintering, J. Eur. Ceram. Soc. 44 (2024) 328–340. https://doi.org/10.1016/j.jeurceramsoc.2023.08.040.
[43] O. Weeger, I. Valizadeh, Y. Mistry, D. Bhate, Inelastic finite deformation beam modeling, simulation, and validation of additively manufactured lattice structures, Addit. Manuf. Lett. 4 (2023) 100111. https://doi.org/10.1016/j.addlet.2022.100111.
[44] C. Manière, G. Kerbart, C. Harnois, S. Marinel, Modeling sintering anisotropy in ceramic stereolithography of silica, Acta Mater. 182 (2020) 163–171. https://doi.org/10.1016/j.actamat.2019.10.032.
[45] M.N. Rahaman, Ceramic Processing and Sintering, 2nd Editio, CRC Press, 2017. https://doi.org/10.1201/9781315274126.
[46] E.A. Olevsky, C. Garcia-Cardona, W.L. Bradbury, C.D. Haines, D.G. Martin, D. Kapoor, Fundamental Aspects of Spark Plasma Sintering: II. Finite Element Analysis of Scalability, J. Am. Ceram. Soc. 95 (2012) 2414–2422. https://doi.org/10.1111/j.1551-2916.2012.05096.x.
[47] C. Manière, L. Durand, A. Weibel, C. Estournès, Spark-plasma-sintering and finite element method: From the identification of the sintering parameters of a submicronic α -alumina powder to the development of complex shapes, Acta Mater. 102 (2016) 169–175. https://doi.org/10.1016/j.actamat.2015.09.003.
[48] C. Manière, E.A. Olevsky, Porosity dependence of powder compaction constitutive parameters: Determination based on spark plasma sintering tests, Scr. Mater. 141 (2017) 62–66.

https://doi.org/10.1016/j.scriptamat.2017.07.026.
[49] C. Manière, C. Harnois, S. Marinel, Porous stage assessment of pressure assisted sintering modeling parameters: a ceramic identification method insensitive to final stage grain growth disturbance, Acta Mater. 211 (2021) 116899. https://doi.org/10.1016/j.actamat.2021.116899.
[50] C. Manière, U. Kus, L. Durand, R. Mainguy, J. Huez, D. Delagnes, C. Estournès, Identification of the Norton-Green Compaction Model for the Prediction of the Ti-6Al-4V Densification During the Spark Plasma Sintering Process, Adv. Eng. Mater. 18 (2016) 1720–1727. https://doi.org/10.1002/adem.201600348.
[51] J.S. Diatta, C. Couder, C. Harnois, S. Marinel, C. Manière, Modeling spark plasma sintering of zirconia with prediction of final stage high densification rate, Mater. Lett. 337 (2023) 133930. https://doi.org/10.1016/j.matlet.2023.133930.
[52] C. Manière, J.S. Diatta, C. Couder, C. Harnois, S. Marinel, Spark plasma sintering grain growth assessment by densification kinetics analysis, Scr. Mater. 228 (2023) 115346. https://doi.org/10.1016/j.scriptamat.2023.115346.
[53] G. Kerbart, C. Harnois, S. Marinel, C. Manière, Modeling the sintering trajectories of MgAl2O4 Spinel, Scr. Mater. 203 (2021) 114048. https://doi.org/10.1016/j.scriptamat.2021.114048.
[54] S.J. Park, S.H. Chung, J.M. Martín, J.L. Johnson, R.M. German, Master Sintering Curve for Densification Derived from a Constitutive Equation with Consideration of Grain Growth: Application to Tungsten Heavy Alloys, Metall. Mater. Trans. A. 39 (2008) 2941–2948. https://doi.org/10.1007/s11661-008-9654-7.
[55] C. Manière, C. Harnois, S. Marinel, Role of microstructure reactivity and surface diffusion in explaining flash (ultra-rapid) sintering kinetics, J. Eur. Ceram. Soc. 43 (2023) 2057–2068. https://doi.org/10.1016/j.jeurceramsoc.2022.12.006.
[56] A. Cabo Rios, E. Olevsky, E. Hryha, M. Persson, R.K. Bordia, Analytical models for initial and intermediate stages of sintering of additively manufactured stainless steel, Acta Mater. 249 (2023) 118822. https://doi.org/10.1016/j.actamat.2023.118822.
[57] C. Manière, T. Zahrah, E.A. Olevsky, Inherent heating instability of direct microwave sintering process: Sample analysis for porous 3Y-ZrO2, Scr. Mater. 128 (2017) 49–52. https://doi.org/10.1016/j.scriptamat.2016.10.008.
[58] J. Zhao, M.P. Harmer, Effect of Pore Distribution on Microstructure Development: I, Matrix Pores, J. Am. Ceram. Soc. 71 (1988) 113–120. https://doi.org/10.1111/j.1151-2916.1988.tb05826.x.
[59] J. Zhao, M.P. Harmer, Effect of Pore Distribution on Microstructure Development: II, First- and Second-Generation Pores, J. Am. Ceram. Soc. 71 (1988) 530–539. https://doi.org/10.1111/j.1151-2916.1988.tb05916.x.
[60] J. Zhao, M.P. Harmer, Effect of Pore Distribution on Microstructure Development: III, Model Experiments, J. Am. Ceram. Soc. 75 (1992) 830–843. https://doi.org/10.1111/j.1151-2916.1992.tb04148.x.
[61] G. Kerbart, C. Manière, C. Harnois, S. Marinel, Predicting final stage sintering grain growth affected by porosity, Appl. Mater. Today. 20 (2020) 100759. https://doi.org/10.1016/j.apmt.2020.100759.
[62] L. Moreno-Sanabria, C. Ramírez, M.I. Osendi, M. Belmonte, P. Miranzo, Thermal conductivity of three-dimensional multi-material core-shell filament structures obtained by material extrusion, Addit. Manuf. 81 (2024) 104018. https://doi.org/10.1016/j.addma.2024.104018.
[63] M. Lakusta, I. Danilenko, G. Volkova, L. Loladze, G. Golovan, I. Brukhanova, V. Glazunova, I. Popov, O. Mazur, T. Konstantinova, Effect of mechanical activation on sintering behaviour of tetragonal zirconia nanopowders, Ceram. Int. 46 (2020) 13953–13960. https://doi.org/10.1016/j.ceramint.2020.02.193.
[64] K. Matsui, A. Matsumoto, M. Uehara, N. Enomoto, J. Hojo, Sintering Kinetics at Isothermal Shrinkage: Effect of Specific Surface Area on the Initial Sintering Stage of Fine Zirconia Powder, J. Am. Ceram. Soc. 90 (2007) 44–49. https://doi.org/10.1111/j.1551-2916.2006.01341.x.
[65] K. Matsui, N. Ohmichi, M. Ohgai, N. Enomoto, J. Hojo, Sintering Kinetics at Constant Rates of Heating: Effect of Al 2 O 3 on the Initial Sintering Stage of Fine Zirconia Powder, J. Am. Ceram. Soc. 88 (2005) 3346–3352. https://doi.org/10.1111/j.1551-2916.2005.00620.x.
[66] J.W. Drazin, R.H.R. Castro, Phase Stability in Nanocrystals: A Predictive Diagram for Yttria–Zirconia, J. Am. Ceram. Soc. 98 (2015) 1377–1384. https://doi.org/10.1111/jace.13504.
[67] J. Le Cloarec, S. Marinel, C. Estournès, M. Dehmas, C. Folton, C. Manière, Stereolithography coupled with spark plasma sintering to produce Ti-6Al-4V complex shapes, J. Manuf. Process. 114 (2024) 122–135. https://doi.org/10.1016/j.jmapro.2024.01.084.
[68] R.M. German, Sintering Theory and Practice, Wiley, Wiley, 1996. http://www.wiley.com/WileyCDA/WileyTitle/productCd-047105786X.html.
[69] H. Tanaka, S. Sawai, K. Morimoto, K. Hisano, Measurement of Spectral Emissivity and Thermal Conductivity of Zirconia by Thermal Radiation Calorimetry., J. Therm. Anal. Calorim. 64 (2001) 867–872. https://doi.org/10.1023/A:1011538022439.